ADVANCED MATERIALS
www.advmat.de

Interstitial Optical Fiber-Mediated Multimodal Phototheranostics Based on an Aggregation-Induced NIR-II Emission Luminogen for Orthotopic Breast Cancer Treatment

Wenguang Zhang, Miaomiao Kang, Xue Li, Hao Yang, Zhijun Zhang, Zhuorong Li, Yibin Zhang, Miaozhuang Fan, Changrui Liao, Chengbo Liu, Gaixia Xu,* Dong Wang,* Zhourui Xu,* and Ben Zhong Tang**

One-for-all phototheranostics based on a single molecule is recognized as a convenient approach for cancer treatment, whose efficacy relies on precise lesion localization through multimodal imaging, coupled with the efficient exertion of phototherapy. To unleash the full potential of phototheranostics, advancement in both phototheranostic agents and light delivery methods is essential. Herein, an integrated strategy combining a versatile molecule featuring aggregation-induced emission, namely tBuTTBD, with a modified optical fiber to realize comprehensive tumor diagnosis and "inside-out" irradiation in the orthotopic breast tumor, is proposed for the first time. Attributed to the intense donor-acceptor interaction, highly distorted conformation, abundant molecular rotors, and loose intermolecular packing upon aggregation, tBuTTBD can synchronously undergo second near-infrared (NIR-II) fluorescence emission, photothermal and photodynamic generation under laser irradiation, contributing to a trimodal NIR-II fluorescence-photoacoustic (PA)-photothermal imaging-guided phototherapy. The tumor treatment is further carried out following the insertion of a modified optical fiber, which is fabricated by splicing a flat-end fiber with an air-core fiber. This configuration aims to enable effective in situ phototherapy by maximizing energy utilization for therapeutic benefits. This work not only enriches the palette of NIR-II phototheranostic agents but also provides valuable insight for exploring an integrated phototheranostic protocol for practical cancer treatment.

1. Introduction

Light, which has had a profound impact on clinical practice in theranostics, has illuminated a new era in cancer therapy.[1] Among diverse light-driven theranostic strategies, multimodal phototheranostics encompassing fluorescence imaging (FLI), photoacoustic imaging (PAI), photothermal imaging (PTI), photothermal therapy (PTT), and photodynamic therapy (PDT) have attracted considerable interest in the research community owing to the real-time imaging with complementary strengths and the in situ therapeutic capabilities.[2,3] Of particular interest are multimodal phototheranostics based on a single molecular species with a defined structure, which significantly reduce the complexities in compositional heterogeneity and intrinsically perform high reproducibility, consequently demonstrating great potential in clinical uses.[4] Nevertheless, the development of such a system remains in its infancy even though tremendous efforts have been made. This is primarily due to the inherently competitive excited-state energy dissipations of each phototheranostic modality in a single molecule.[5] Moreover, phototheranostics is usually subjected to the tissue extinction of the excitation light, typically limiting their use to superficial and localized tumors.[3,6–8] To overcome this shortcoming, interstitial optical fibers featuring hair-like dimensions, flexibility, and biocompatibility have emerged as a promising solution. These fibers can transport photons end-to-end without

W. Zhang, Y. Zhang, M. Fan, G. Xu, Z. Xu
School of Biomedical Engineering
Shenzhen University Medical School
Shenzhen University
Shenzhen, Guangdong 518055, China
E-mail: xugaixia@szu.edu.cn; xuzhouray@szu.edu.cn

The ORCID identification number(s) for the author(s) of this article can be found under https://doi.org/10.1002/adma.202406474

DOI: 10.1002/adma.202406474

M. Kang, X. Li, H. Yang, Z. Zhang, D. Wang, B. Z. Tang
Center for AIE Research
Guangdong Provincial Key Laboratory of New Energy Materials Service Safety
College of Materials Science and Engineering
Shenzhen University
Shenzhen 518060, P. R. China
E-mail: zhijunzhang@szu.edu.cn; wangd@szu.edu.cn; tangbenz@cuhk.edu.cn

energy loss, providing excellent opportunities for the "inside-out" manner of laser irradiation, thus breathing new life into the field of phototheranostics.[9] Evidently, exploring advanced phototheranostic protocols that incorporate both one-for-all phototheranostic agents and the interstitial optical fiber is an appealing yet significantly challenging task.

Luminogens with aggregation-induced emission characteristics (AIEgens) have currently emerged as ideal candidates for the development of multimodal phototheranostic agents. This is due to the abundance of rational and/or vibrational groups on the molecular backbone, which serves as a convenient knob to finely adjust the energy flow upon excitation.[5,10] Specifically, intense intramolecular motions can efficiently dissipate absorbed light energy as heat[11] while constraints on these motions can guide the energy toward the intersystem crossing (ISC) process or photoluminescence.[12] Of particular interest, FLI in the second near-infrared window (NIR-II, 1000–1700 nm) has garnered significant attention due to minimum tissue light extinction, low autofluorescence interference, minimum collateral damage, and high sensitivity.[13] These characteristics enabled it to provide abundant details at the pathological sites.[8,14,15] Therefore, developing NIR-II AIEgens holds great promise for further advancements in phototheranostics.

In this contribution, we, for the first time, advanced light-driven tumor therapy by taking advantage of both the NIR-II emissive phototheranostic agent and the light delivery method (**Scheme 1**). By strengthening the electron donor-acceptor (D–A) interaction on a highly twisted conjugate skeleton, we successfully synthesized a multimodal phototheranostic AIEgen agent, namely tBuTTBD, which features NIR absorption, NIR-II emission, remarkable PA signal, prominent photothermal effect, and satisfactory reactive oxygen species (ROS) generation under laser irradiation at 808 nm. Facilitated by amphiphilic polymers and the surface modification of iRGD, tBuTTBD nanoparticles-iRGD (NPs-iRGD) could efficiently target tumor sites after intravenous injection, as evidenced by the light-triggered NIR-II FLI-PAI-PTI trimodal imaging. In situ phototherapy of orthotopic breast tumor was initiated using a modified optical fiber (Scheme 1d), which was fabricated by splicing a flat-end optical fiber with an air-core fiber end to maximize the laser diffusion within the tumor. This approach demonstrated superior therapeutic efficacy to conventional phototherapy methods utilizing laser irradiation through a collimator. The biosafety of tBuTTBD NPs-iRGD was further validated through a comprehensive assessment. This work proposes a fantastic combination of phototherapeutic agents and the light delivery method, not only to circumvent the biological light barriers on the body but also to unleash the full potential of phototheranostics, paving the way for advancements in clinical applications.

2. Results and Discussion

2.1. Molecular Design and Photophysical Property Studies

Tert-butyl-substituted diphenylamine serves as a strong electron donor, sterically encumbered hexylthiophene acts as a π-bridge and the additional electron donor, and highly electron-withdrawing benzobisthiadiazole works as the strong acceptor, thus constructing the compound tBuTTBD (Scheme 1a). Thereinto, the propeller-like conformation of tert-butyl-substituted diphenylamine, the steric hindrance from tert-butyl groups, as well as the long alkyl chains of hexylthiophene jointly distorted the whole molecular skeleton that not only restrains the fluorescence quenching during aggregation by significantly diminishing the intermolecular π-π stacking and the interactions with water but also provides sufficient space for intramolecular motions, benefiting the non-radiative thermal energy decays. In addition, the strong D–A effect along tBuTTBD is expected to reduce the electronic band gap and improve the ISC process, leading to bathochromic-shift absorption and emission wavelengths as well as good photodynamic potential (Scheme 1b). The synthetic route of tBuTTBD is presented in Scheme S1 (Supporting Information), and the chemical structure of the product is confirmed by nuclear magnetic resonance spectroscopy (^{1}H NMR, ^{13}C NMR) and high-resolution mass spectrometry (HRMS), as shown in Figures S1–S6 (Supporting Information).

To gain insights into the chemical structure of tBuTTBD, density functional theory (DFT) calculations with the Gaussian 09 program at the B3LYP/6-31G(d) level were conducted. In Figure S7 (Supporting Information), large dihedral angles exceeding 50° are observed between the diphenylamine and hexylthiophene, as well as between the hexylthiophene and benzobisthiadiazole. These findings highlight the torsional structure of tBuTTBD and its capacity to inhibit molecular π-π stacking upon aggregation. The molecular orbitals of tBuTTBD were further studied. As illustrated in Figure S8 (Supporting Information), the highest occupied molecular orbital (HOMO) is primarily located on the electron donors, whereas the lowest unoccupied molecular orbital (LUMO) is mainly distributed over the acceptor moiety. This indicates an efficient internal charge transfer (ICT) and the typical D–A interaction. Furthermore, the energy gap (ΔE_g) of tBuTTBD was measured to be 1.38 eV, a value comparable to those organic molecules exhibiting NIR absorption.[14,16,17]

Z. Li, C. Liao
Shenzhen Key Laboratory of Photonic Devices and Sensing Systems for Internet of Things
Guangdong and Hong Kong Joint Research Centre for Optical Fiber Sensors
State Key Laboratory of Radio Frequency Heterogeneous Integration
Shenzhen University
Shenzhen 518060, China

Z. Li, C. Liao
Shenzhen Key Laboratory of Ultrafast Laser Micro/Nano Manufacturing
Key Laboratory of Optoelectronic Devices and Systems of Ministry of Education/Guangdong Province
College of Physics and Optoelectronic Engineering
Shenzhen University
Shenzhen 518060, China

C. Liu
Research Laboratory for Biomedical Optics and Molecular Imaging
Key Laboratory of Biomedical Imaging Science and System
Shenzhen Institute of Advanced Technology
Chinese Academy of Sciences
Shenzhen 518055, China

B. Z. Tang
School of Science and Engineering
Shenzhen Institute of Aggregate Science and Technology
The Chinese University of Hong Kong
Shenzhen (CUHK-Shenzhen), Guangdong 518172, China

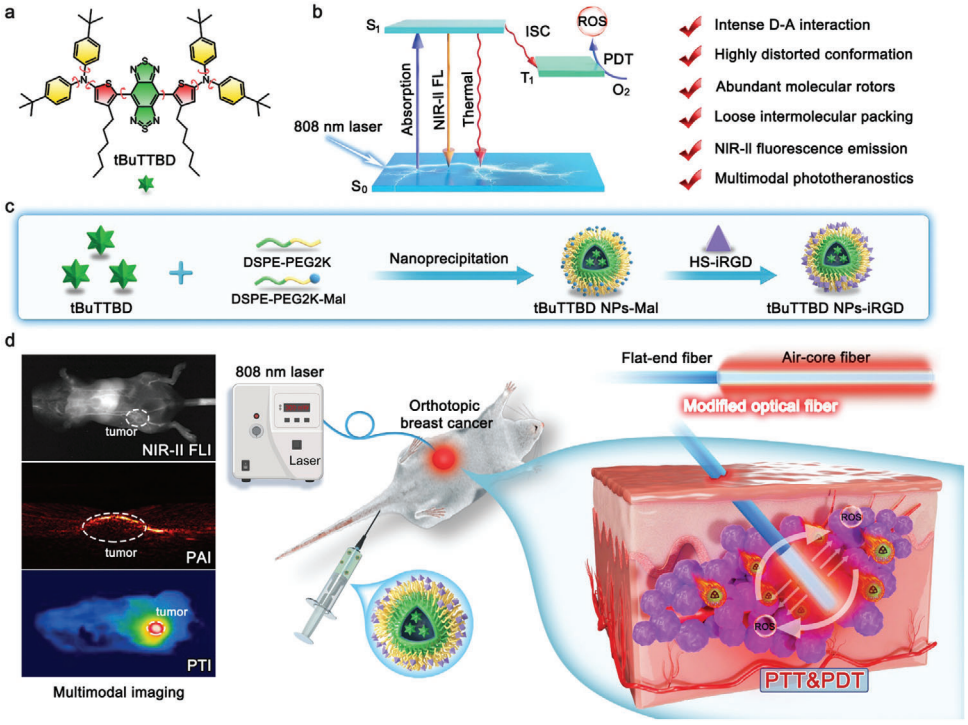

Scheme 1. Schematic illustration of molecular design principle, preparation of nanoparticles (NPs), and phototheranostic applications. a) Molecular structure and b) energy decay pathways of tBuTTBD. c) Preparation process of iRGD-decorated NPs. d) Interstitial optical fiber-mediated phototherapy guided by trimodal imaging.

The optical properties of tBuTTBD molecules were characterized using UV-Vis-NIR and fluorescence spectroscopies. As shown in **Figure** 1a, the maximum absorbance of tBuTTBD in THF is at 812 nm and the maximal emission peak occurs at 1088 nm. Such a long emission peak of tBuTTBD is attributed to the exceptionally strong D–A interaction and extended π-conjugation, well matching the concept of molecular design. The AIE feature of tBuTTBD was then investigated by analyzing the FL spectra in THF/water mixtures with varying water fractions (f_W) (Figure S9, Supporting Information). tBuTTBD demonstrates rather faint emission in pure THF solvent due to the energy consumption dominated by the intramolecular motions. As the f_W increases, the emission intensities of tBuTTBD increase gradually due to the restriction of intramolecular motions (RIM) effect, showing the typical AIE feature (Figure 1b). To endow tBuTTBD with water-dispersity and tumor-targeting ability, amphiphilic polymers DSPE-PEG2K and DSPE-PEG2K-Mal were employed as the carrier molecules to fabricate AIEgen NPs using a nanoprecipitation method. Subsequently, the NPs surface was modified with iRGD (Scheme 1c), known for its ability to penetrate deep into tumors for enhanced therapeutic purposes.[18] Dynamic light scattering (DLS) measurements revealed that the hydrodynamic sizes of tBuTTBD NPs-Mal and tBuTTBD NPs-iRGD were 62.41 and 67.14 nm (Figure S10, Supporting Information; Figure 1c), respectively. The difference in the hydrodynamic size confirmed the successful attachment of iRGD on the surface of NPs, a fact further corroborated by the significant difference in zeta potential (Figure S11, Supporting Information). The encapsulation efficiency of tBuTTBD was calculated to be ≈90% (Figure S12, Supporting Information). In addition, tBuTTBD NPs-iRGD maintained their absorbance and size in H_2O, PBS, and culture medium solutions over 6 days, suggesting high storage stability (Figure S13, Supporting Information).

The tBuTTBD NPs-iRGD exhibited an absorbance maximum of 808 nm and an emission peak of 1092 nm (Figure S14, Supporting Information), similar to that of tBuTTBD in THF. tBuTTBD NPs-iRGD exhibited exceptional photostability, showing minimal changes in the absorbance spectrum after continuous laser irradiation for 30 mins (Figure 1d), much more robust than AuNRs and ICG (Figure S15, Supporting Information). Such a feature is satisfactory to light-driven bioapplications. The AIE effect endows the tBuTTBD NPs-iRGD with a higher fluorescence quantum yield of 0.8% than the commercial IR-26 dye (0.5%) (Figure S16, Supporting Information), benefiting the NIR-II fluorescence imaging (Figure 1e). A linear relationship between the NIR-II FL intensities and the concentration of NPs has been further concluded, which could roughly indicate the biodistribution of NPs (Figure S17, Supporting Information).

The photothermal effect of tBuTTBD NPs-iRGD was evaluated under 808 nm laser irradiation. tBuTTBD NPs-iRGD achieved a temperature increment of 16 °C at merely 50 μM under a low power density of 0.4 W cm^{-2}. The heat conversion efficiency was determined to be 58.9% (Figure S18, Supporting Information), surpassing that of most reported photothermal agents.[19] In addition, the photothermal performance of tBuTTBD NPs-iRGD can be well-adjusted by varying the power density of the 808 nm laser (Figure S19, Supporting Information) and the concentration of tBuTTBD NPs-iRGD (Figure S20, Supporting

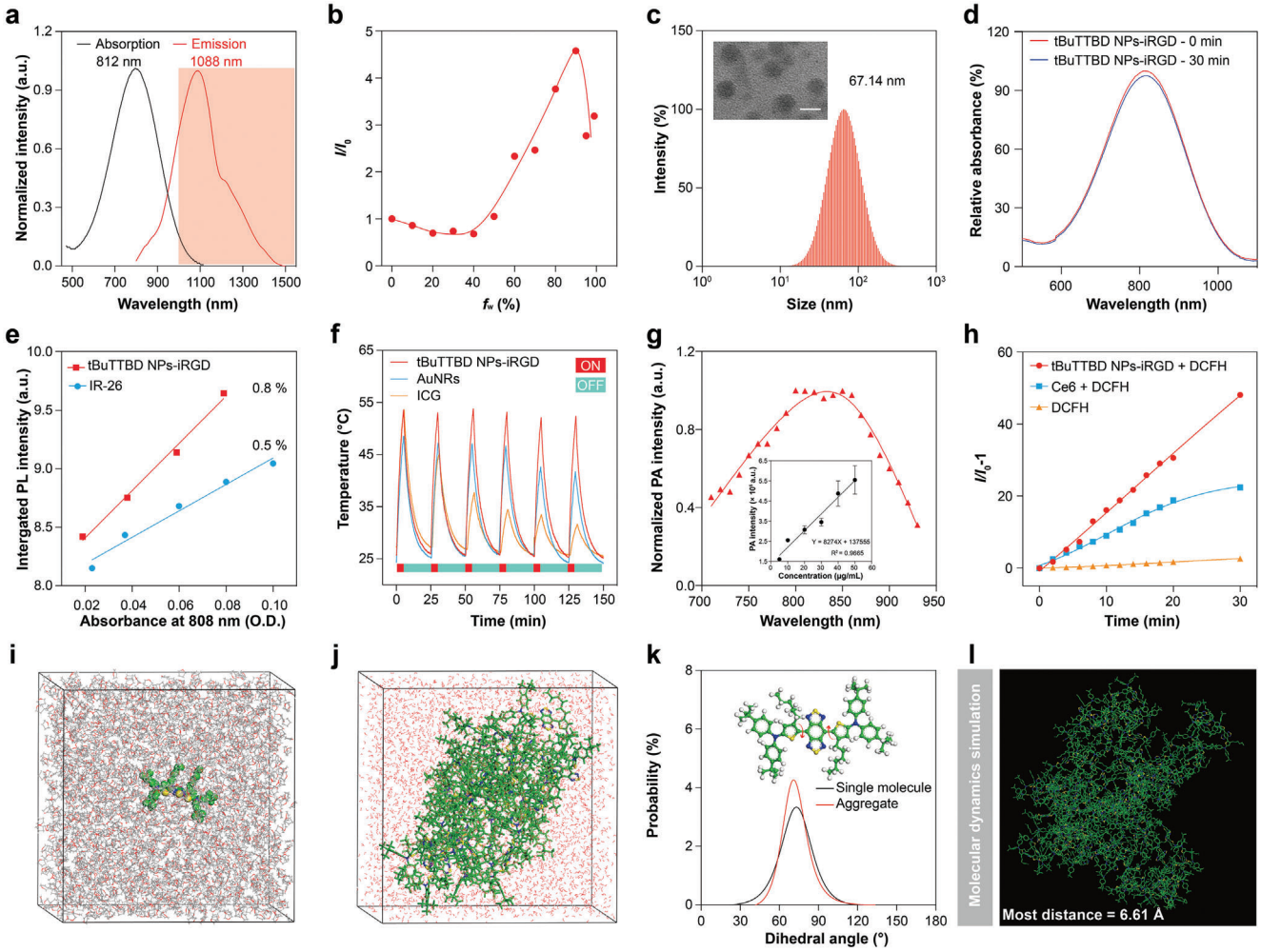

Figure 1. a) Normalized absorption and PL spectra of tBuTTBD in THF. b) Plots of the relative emission intensity (I/I_0) versus f_W, I, and I_0 are the PL peak values of tBuTTBD in the THF and THF/H_2O mixture, respectively. c) Size distribution and TEM image of tBuTTBD NPs-iRGD. d) Relative absorbance of tBuTTBD NPs-iRGD before and after 30 min of laser irradiation (808 nm, 0.4 W/cm^2). e) Relative fluorescence quantum yield of tBuTTBD NPs-iRGD. f) Photothermal stability evaluation of tBuTTBD NPs-iRGD under six on-off laser irradiation (808 nm, 0.4 W cm^{-2}). g) Normalized PA spectrum of tBuTTBD NPs-iRGD. h) Photodynamic effect of tBuTTBD NPs-iRGD under laser irradiation (808 nm, 0.4 W cm^{-2}). Molecular dynamics simulation snapshot of i) a single tBuTTBD molecular disperser in THF and j) tBuTTBD aggregates in H_2O. k) Dihedral angle (between the hexylthiophene and benzobisthiadiazole) distributions of the single-dispersed molecule (THF solution) and the innermost molecule of the aggregate (water solution). l) Simulation of the intermolecular distance of tBuTTBD in nanoaggregates.

Information), implying the high sensitivity of photothermal transduction. The photothermal stability of tBuTTBD NPs-iRGD was further assessed in comparison to commercial photothermal agents, AuNRs and ICG. This evaluation involved subjecting the samples to six consecutive laser irradiation and natural cooling cycles (Figure 1f). The photothermal profiles of tBuTTBD NPs-iRGD were nearly unchanged and reversible in each cycle, in sharp contrast to the degenerated profiles of AuNRs and ICG. Encouraged by the great photothermal performance, the PA properties of tBuTTBD NPs-iRGD were further examined. The PA spectrum of tBuTTBD NPs-iRGD was well-matched with the absorption spectrum, peaking near 808 nm (Figure 1g). A linear relationship between the PA intensities and concentrations of AIEgen has been concluded (Figure S21, Supporting Information) and good PA stability has been verified (Figure S22, Supporting Information), demonstrating its great potential for in vivo PA imaging and semi-quantitative analysis. A good photodynamic effect has also been realized by tBuTTBD NPs-iRGD under 808 nm laser irradiation. 2′,7′-dichlorodihydrofluorescein (DCFH) was used to examine the production of the overall ROS. As demonstrated in Figure 1h, the fluorescence of DCFH increases obviously under laser irradiation (0.4 W cm^{-2}) in the presence of tBuTTBD NPs, demonstrating its good ROS production. Such a production rate is superior to the commercial photosensitizer Ce6 (Figure S23, Supporting Information). Furthermore, the ROS type was examined by Electron Spin Resonance (ESR) spectroscopy. As shown in Figure S24 (Supporting Information), hydroxyl, and superoxide radicals are the dominant ROS generated by tBuTTBD NPs-iRGD under laser irradiation. The additional photodynamic feature makes tBuTTBD an efficient phototherapeutic agent for collaborative cancer therapy.

A molecular dynamics simulation was conducted to decipher the superiority of the photothermal response of tBuTTBD NPs-iRGD. The dihedral angles of tBuTTBD in THF (Figure 1i) and water (Figure 1j) were calculated and compared. As depicted in Figure 1k, the dihedral angles between the hexylthiophene and benzobisthiadiazole in both monodisperse and aggregate states are notably large and almost identical, suggesting strong resistance to π-π stacking upon aggregation. A similar situation has also been observed at the dihedral angles between the hexylthiophene and tert-butyl-substituted diphenylamine of tBuTTBD (Figure S25, Supporting Information). Subsequently, an assessment was carried out on the distribution of the nearest distance between the center of tBuTTBD in its aggregated state within a water-filled environment was evaluated. Back to the equilibrium state after 800 ns, tBuTTBD molecules were randomly aggregated in the simulation space with a distance of the maximum proportion at 6.61 Å (Figure 1l). Such distance is exceptionally large compared to the previously reported AIEgens[16,20] and is believed to be related to tert-butyl groups and hexyl chains, which provide significant spatial hindrance. The dihedral angles observed in the aggregated states, coupled with the notably large intermolecular distances, support the presence of active intramolecular motions of tBuTTBD within the NPs. This dynamic behavior ensures efficient heat dissipation upon irradiation, contributing to the photothermal and PA responses.

2.2. Preparation of Modified Optical Fiber for Light Delivery

Thorough light irradiation in biological tissues is essential to boost the phototheranostics. To achieve this goal, a flat-cut end fiber was spliced with an air-core fiber end to efficiently promote laser diffusion, due to the mismatch in the light guiding modes. To further promote the light diffusion to the air, epoxy resin was used and coated on the fiber end (**Figure 2**a). As shown in Figure 2b, such structure configuration enables efficient light diffusion after multiple internal reflections and refractions. Furthermore, air-core fiber with different diameters was used to optimize the performance of the modified optical fibers. Numerical simulations of the light field revealed that a larger amount of light energy can diffuse out of the fiber end as the diameter of the air-core fiber increases (Figure 2c). The experimental results were coincident with the simulation predictions (Figure 2e). In addition, the epoxy resin coating significantly increased the light diffusion extent at the fiber end (Figure 2f). It should be noted that only half of the energy from the side surface can be captured owing to the configuration of the optical power meter. Thus, the overall light power from the fiber end was nearly the same as that from the collimator, implying that almost all the laser light was emitted. The optimized optical fiber is subsequently fabricated and emits laser light as demonstrated in Figure 2d.

The photothermal responses of tBuTTBD NPs-iRGD irradiated through a modified optical fiber were subsequently conducted (Scheme S2, Supporting Information). The temperature increments were increased as the laser power and the concentration of tBuTTBD increased (Figure 2g,h), similar to the photothermal profiles of tBuTTBD NPs-iRGD irradiated through a collimator. However, it should be noted that the maximum temperatures of samples after 10 min of irradiation through the modified optical fiber were always slightly smaller than that achieved using a collimator with the same laser power of 300 mW and NPs concentration. Further careful observation under the thermal imaging system found that extensive heat is generated at only the upper half of the sample under laser irradiation using a collimator. By sharp contrast, homogeneous heat generation in the sample solution was realized under the laser irradiation from the modified optical fiber (Figure 2i). This phenomenon can be well explained by two reasons: 1) the "inside-out" manner of laser irradiation through a modified optical fiber is capable of illuminating a greater space; 2) heating more liquid volume with the same irradiation energy will inevitably lower the final equilibrium temperature. Therefore, we anticipate a greater potential and opportunity for phototherapy using a modified optical fiber, since a larger volume in target tissues becomes accessible for treatment.

Additional experiments were conducted with mice skin and chicken breast tissue as the light barriers to simulate heat generation inside the body (Scheme S3, Supporting Information). The mice's skin was first used to cap on the solution surface of samples to block the "outside-in" irradiation. As shown in Figure 2j, the photothermal response triggered by modified optical fiber is not affected at all owing to the "inside-out" manner of irradiation. Conversely, the temperature increments of samples irradiated using a collimator were significantly lower due to the severe light attenuation. Then, chicken breast tissue was used as another light barrier to simulate the biological tissue of mice. In the collimator group, a tissue layer with a thickness of 1 mm was capped on the sample surface. In the fiber group, a modified optical fiber was penetrated inside a cylindrical shape of tissue with a diameter of 1 mm. It should also be mentioned that the surface coating of epoxy resin can strengthen the toughness and increase the biocompatibility of the optical fiber, facilitating in vivo photothermal therapy. As demonstrated in Figure 2k, the fiber group still outperforms the collimator group according to the thermal infrared images. These results manifested the great potential of the modified optical fiber in photothermal therapy. In addition, the photodynamic effect of tBuTTBD NPs-iRGD was also examined via a modified optical fiber. As shown in Figure 2l, evident ROS production was enabled by the NPs, which is also much more potent than that achieved by Ce6.

2.3. Cellular Uptakes, Cytotoxicity Assay, and In Vitro Phototherapy

iRGD peptide was used to endow tBuTTBD NPs with tumor-targeting ability.[18,21] Flow cytometry analysis was performed to evaluate the cellular uptake of tBuTTBD NPs and tBuTTBD NPs-iRGD by 4T1 cells across diverse concentrations in order to assess the targeting capability. Due to the mismatch between the NIR-II emission of tBuTTBD and the detection wavelength range of the flow cytometer, both tBuTTBD NPs and tBuTTBD NPs-iRGD were co-loaded with 20% of DPTA-BT, a highly emissive AIE molecule designed by our previous work.[7] As shown in **Figure 3**a, the mean fluorescence intensities (MFI) of cells increase either with a higher concentration of NPs or the existence of iRGD. The targeting ability of tBuTTBD NPs-iRGD was further confirmed across a broader range of NPs concentrations (from 1 to 50 μM based on tBuTTBD) (Figure S26, Supporting

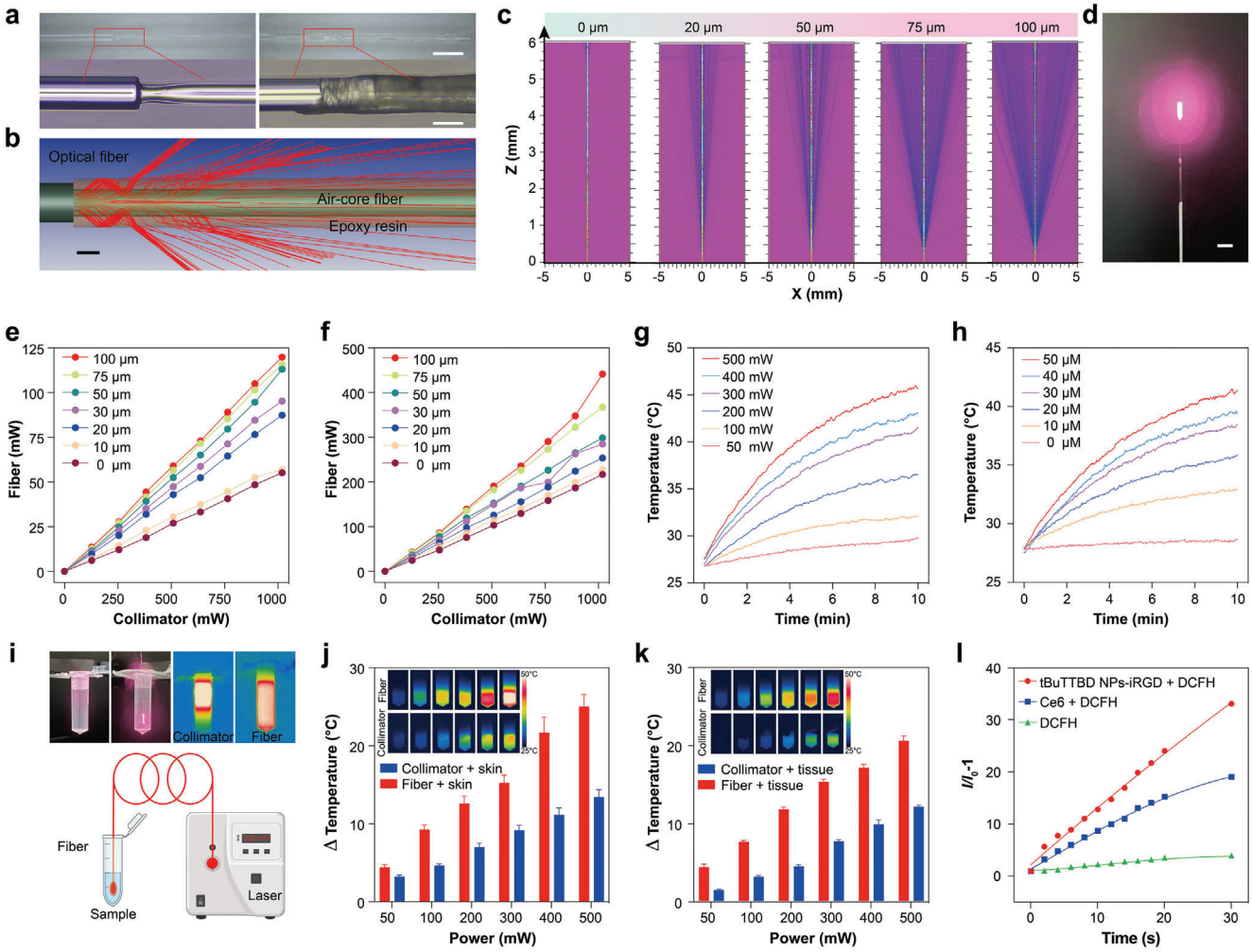

Figure 2. a) Images of spliced optical fiber without and with epoxy resin coating. Scale bar: 1 mm and 200 μm. b) Numerical simulation of light transmission path from the fiber end. Scale bar: 100 μm. c) Numerical simulation of light field emitted from the fiber end. d) Laser emission from the optimized optical fiber. Scale bar: 5 mm. The power of laser light emitted from the fiber end e) without and f) with epoxy resin coating. Photothermal profiles of tBuTTBD NPs-iRGD g) irradiated with different power densities and h) at different NPs concentrations through a modified optical fiber (808 nm, 300 mW). i) Schematic illustration of heat generation induced by the collimator and modified optical fiber in the presence of tBuTTBD NPs-iRGD. Temperature increment of tBuTTBD NPs-iRGD samples under laser irradiation through a collimator and modified optical fiber with j) skin or k) chicken breast tissue as the light barrier. l) Photodynamic effect of tBuTTBD NPs-iRGD under laser irradiation through a modified optical fiber (808 nm, 300 mW).

Information). The confocal laser scanning microscopy (CLSM) showed that tBuTTBD NPs-iRGD exhibited stronger red fluorescence than tBuTTBD NPs, indicating more efficient cellular uptakes by 4T1 cells (Figure 3b; Figure S27, Supporting Information). Furthermore, the red fluorescence emitted by NPs overlapped with the green fluorescence of LysoTracker Green, producing yellow spots in the merged pictures. The intensity line profile of the region indicated by a red arrow in Figure 3b, revealed a comparable diameter between the red and green dots, suggesting that endocytosis is responsible for cellular uptake (Figure 3c). The endocytic pathways were then evaluated by flow cytometry analysis using various pathway inhibitors (Figure S28, Supporting Information). An energy-dependent endocytosis procedure of the NPs has been observed since the cellular uptake efficiency can be efficiently inhibited at 4 °C, by chlorpromazine (clathrin-mediated endocytosis inhibitor) and nystatin (caveolae/lipid-mediated endocytosis inhibitor) (Figure 3d). What is more, the inhibitory effect of chlorpromazine was more effective than that of nystatin, indicating the dominant pathway of clathrin-mediated endocytosis.

In vitro phototherapy of tBuTTBD NPs-iRGD was assessed subsequently using 4T1 cells. First, four cell lines (4T1, 293T, HS578bst, and GL261) were cultured and incubated with tBuTTBD NPs-iRGD for 12 or 24 h to evaluate the dark cytotoxicity. The survival rates of all the investigated cells reached more than 87% at different concentrations of NPs and incubation time (Figure S29, Supporting Information), demonstrating the great biocompatibility and negligible dark cytotoxicity of tBuTTBD NPs-iRGD. In vitro phototherapy induced by an 808 nm laser with an output power of 300 mW was then performed on

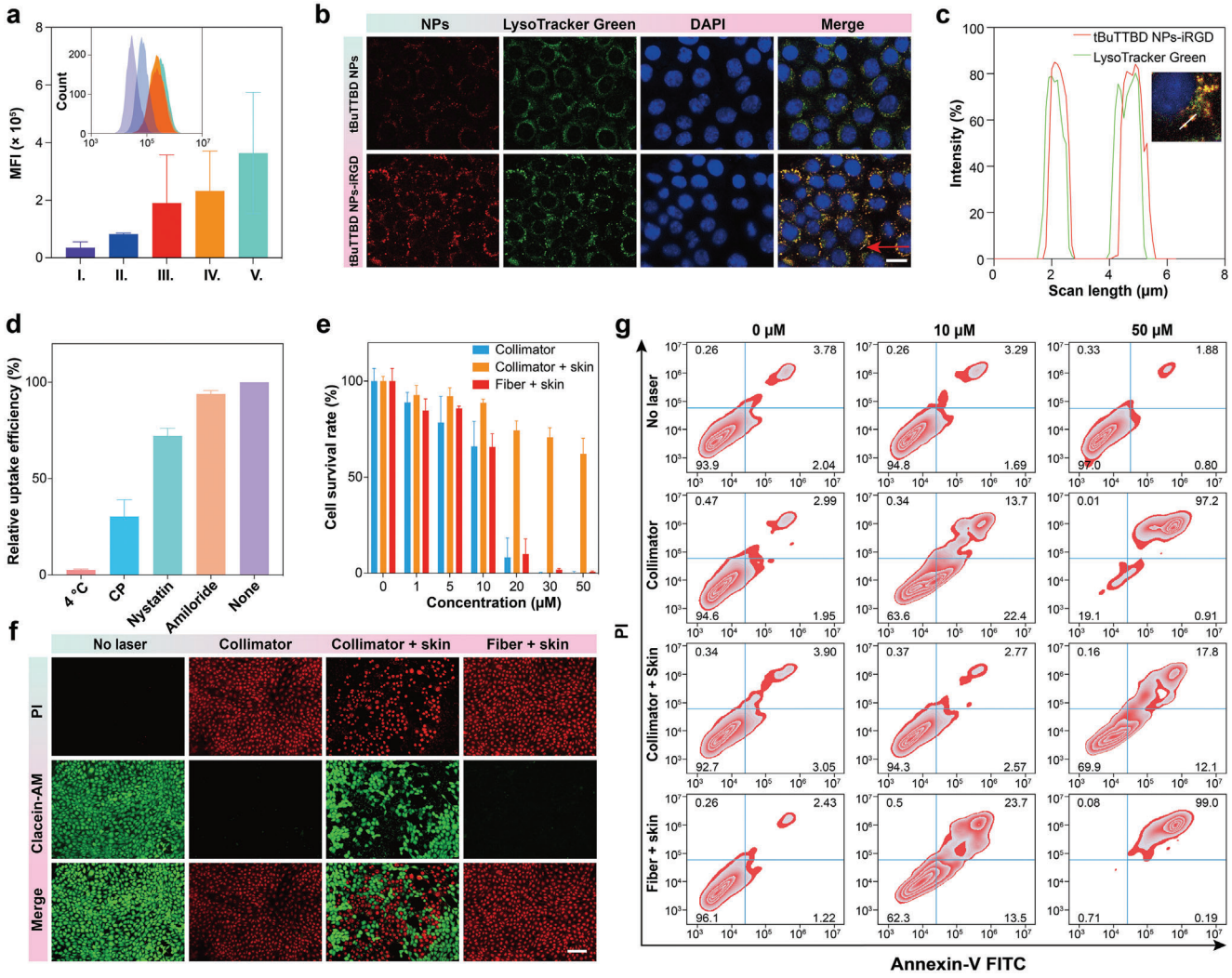

Figure 3. a) Flow cytometry analysis of cellular uptakes of tBuTTBD NPs and tBuTTBD NPs-iRGD. I: PBS; II: tBuTTBD NPs of 10 μM; III: tBuTTBD NPs-iRGD of 10 μM; IV: tBuTTBD NPs of 50 μM; V: tBuTTBD NPs-iRGD of 50 μM. b) Intracellular localization of tBuTTBD NPs and tBuTTBD NPs-iRGD co-loaded with a reported red probe named DPTA-BT for convenient observation by CLSM. Scale bar: 20 μm. c) Line profile of selected endosomes. d) Relative uptake efficiency of 4T1 cells with different treatments. CP: chlorpromazine. e) Cell survival rate of 4T1 cells incubated with various concentrations of tBuTTBD NPs-iRGD with different laser treatments. f) Live/dead cell staining of 4T1 cells after various treatments. Scale bar: 100 μm. g) Apoptosis analysis of 4T1 cells after various treatments.

4T1 cells in the presence of tBuTTBD NPs-iRGD (Scheme S4, Supporting Information). Using the conventional way of irradiation through a collimator with the same output power of 300 mW, tBuTTBD NPs-iRGD can efficiently inhibit the growth of cancer cells even at a relatively low concentration (less than 10 μM) (Figure 3e). The mouse's skin was further covered on the culture plate to simulate the light barrier during the phototherapy. In this case, the treatment efficacy of tBuTTBD NPs-iRGD triggered through a collimator was attenuated significantly, with over 62.1% of cells remaining alive even at a higher concentration of 50 μM. In sharp contrast, a modified optical fiber can ignore light obstruction by the skin, thereby maintaining the strong curative effect of tBuTTBD NPs-iRGD. The Calcein-AM/PI double staining was used to further demonstrate the therapeutic outcomes of tBuTTBD NPs-iRGD across various concentrations irradiated under different conditions (Figure S30, Supporting Information). As exhibited in Figure 3f, nearly all cells were eradicated under laser irradiation through a collimator with strong and massive red fluorescence appeared. As the mouse's skin blocked the incident light, extensive green fluorescence remained, implying the sharply weakened treatment efficacy of tBuTTBD NPs-iRGD. These results simultaneously proved the excellent therapeutic efficacy of tBuTTBD NPs-iRGD and highlighted the superiority of a modified optical fiber.

Annexin V-FITC/PI detection assay was further employed on 4T1 cells after different treatments to elucidate the cell death mechanism. Almost all the 4T1 cells remain viable in the absence of tBuTTBD NPs-iRGD or in the group treated with the tBuTTBD NPs-iRGD group but without laser irradiation (Figure 3g). This suggests that all the light delivery methods and the NPs themselves were biocompatible enough to avoid undesired cell damage. When phototherapy was introduced via a collimator, early

and late apoptosis of 4T1 cells was observed, and over 97% of late apoptosis dominated the cell death mode when 50 μM of AIEgens was used. Such cell apoptosis was largely weakened as the mouse's skin blocked the laser from the collimator. However, the modified optical fiber can avoid light blockage by the skin and induce 99% late apoptosis after treatment.

2.4. Multimodality Imaging of Tumors and In Vivo Phototherapy

Encouraged by the excellent versatility of tBuTTBD NPs-iRGD, multimodal imaging, including NIR-II FLI, PAI, and PTI, was performed on tumor-bearing mice to study the biodistribution of the NPs after intravenous injection. As illustrated in **Figure 4a**, the fluorescence intensities at the tumor site increased significantly in the first 24 h, followed by a slight decay attributed to the tissue metabolism. It can be noted that the tumor vasculatures were distinguished well right after the injection of the NPs (Figure 4b; Figure S31, Supporting Information). Blood vessels with 2.2 and 3.6 μm diameters and signal-to-background (SBR) ratios of 7.5 and 6.6 were clearly visualized, showing good imaging quality of NIR-II light (Figure 4c,d). However, at 24 h post-injection, these vessels became indistinguishable, and strengthened fluorescence at the tumor region was observed, suggesting the enhanced permeation and retention (EPR) effect of tBuTTBD NPs-iRGD. At 36 h post-injection, the mice's major organs and tumors were collected for NIR-II imaging. Bright fluorescence is still emitted from the tumor (Figure S32, Supporting Information), confirming the good targeting ability of tBuTTBD NPs-iRGD toward tumor tissues. Attributed to the remarkable photothermal effect of tBuTTBD NPs-iRGD, PAI and PTI were performed on the tumor-bearing mice after NPs injections. As shown in Figure 4f, the PA signals were gradually strengthened at the tumor sites in the first 24 h and then slightly decayed in the next 12 h. Such intensity dynamics are similar to those observed under NIR-II FLI (Figure 4e). In addition, the tumor vasculatures can be distinguished well through the PAI at 5 min post-injection of tBuTTBD NPs-iRGD (Figure S33, Supporting Information). For PTI, mice were irradiated with an 808 nm laser (300 mW) and monitored via a thermal camera. Efficient therapeutic temperature at the tumor site was observed between 12 h and 36 h post-injection after laser irradiation (Figures S34 and S35, Supporting Information). Taken together, the results of multimodal imaging not only confirmed the tumor-targeting ability of tBuTTBD NPs-iRGD but also suggested the appropriate time to perform phototherapy.

Then, tBuTTBD NPs-iRGD was used as the phototherapeutic agent for tumor therapy. BALB/c mice bearing 4T1 tumors were randomly divided into five groups: VI: PBS; VII: tBuTTBD NPs-iRGD; VIII: PBS plus NIR laser via a modified optical fiber; IX: tBuTTBD NPs-iRGD plus NIR laser via a collimator; X: tBuTTBD NPs-iRGD plus NIR laser via a modified optical fiber. A single intravenous administration was carried out during the treatment session, followed by a single session of laser irradiation (808 nm, 300 mW, 10 min) at 12 h post-injection. In groups VIII and X, the modified optical fibers were penetrated into tumors with an average depth of 5 mm (Figure 4g). The whole tumor was illuminated when the laser was turned on. Ultrasound imaging revealed the spatial position of the modified optical fiber inside the tumor (Figure S36, Supporting Information). Remarkably, intense temperature increment on the tumor site has been observed in group X with a maximum temperature of 54 °C, in contrast to the maximum temperature of 50 °C in group IX (Figure 4h). The insertion of the modified optical fiber into the tumor can efficiently avoid light attenuation by the skin and healthy biological tissues. Therefore, more light energy can be utilized by tBuTTBD NPs-iRGD for heat generation. In addition, the temperature increment in group VIII only reached 39 °C, implying the negligible photothermal effect of the modified optical fiber in the absence of tBuTTBD NPs-iRGD. The detailed thermal infrared images are summarized in Figure S37 (Supporting Information). Moreover, the mice's weight and tumor volume in each group were recorded every 2 days during the therapeutic process. No significant difference in body weight has been observed among different groups (Figure S38, Supporting Information), indicating no severe side effects caused by the therapeutic procedures. The tumor growth curves in Figure 4i solidly demonstrated the remarkable therapeutic outcomes in group X. Specifically, tumors in group X barely grew after phototherapy assisted with a modified optical fiber. In sharp contrast, groups without phototherapy effect grew totally out of control (Figure 4j). It should be noted that the tumor growth in group IX was inhibited to a relatively mild extent. Such therapeutic outcomes matched well with the temperature increment in Figure 4b and implied the negative influence of biological tissue on phototherapy. The tumor weights further confirmed the highly efficient therapeutic effect of tBuTTBD NPs-iRGD activated by NIR laser via a modified optical fiber (Figure S39, Supporting Information).

After complete treatment of 12 days, all mice were sacrificed, and tumors were collected for histological analysis. As demonstrated in Figure S40 (Supporting Information), hematoxylin and eosin (H&E) staining of tumor slices clearly shows that tBuTTBD NPs-iRGD activated by NIR laser (group IX and X) could induce severe damage to the tumor tissues due to local hyperthermia and ROS. This resulted in loosely arranged tumor cells with significantly increased cavities and remarkable conspicuous karyopyknosis. By contrast, group VI-VIII exhibited an abundance of densely arranged tumor cells. TdT-mediated dUTP nick end labeling (TUNEL) immunofluorescence staining assay further confirmed serious apoptosis in the tumor tissues of mice treated with NIR laser irradiation in the presence of tBuBBTD NPs-iRGD. In addition, Ki67-positive proliferating cells and CD31-positive vessel formation signals were nearly absent in groups IX and X, further revealing the efficient phototherapeutic effect and tumor-inhibited growth. In sharp contrast, massive cell proliferation and angiogenesis appeared in the negative control groups (groups VI-VIII). Histological analysis with a larger field of view of the tumor was performed to study the death mechanism of phototherapy. As shown in Figure 4k, tumor cells without photothermal and photodynamic treatments (groups VI-VIII) demonstrated good proliferation, as indicated by the extensive Ki67-positive green fluorescence. In the case of phototherapy induced by laser through a collimator (group IX), the outer region of the tumor did not exhibit any Ki67 fluorescent signals. Conversely, the inner portion of the tumor, which was expected to receive less laser exposure, remained Ki67 positive. Remarkably, all cells were killed in group X without Ki67-positive green fluorescence throughout the view. These results again highlighted

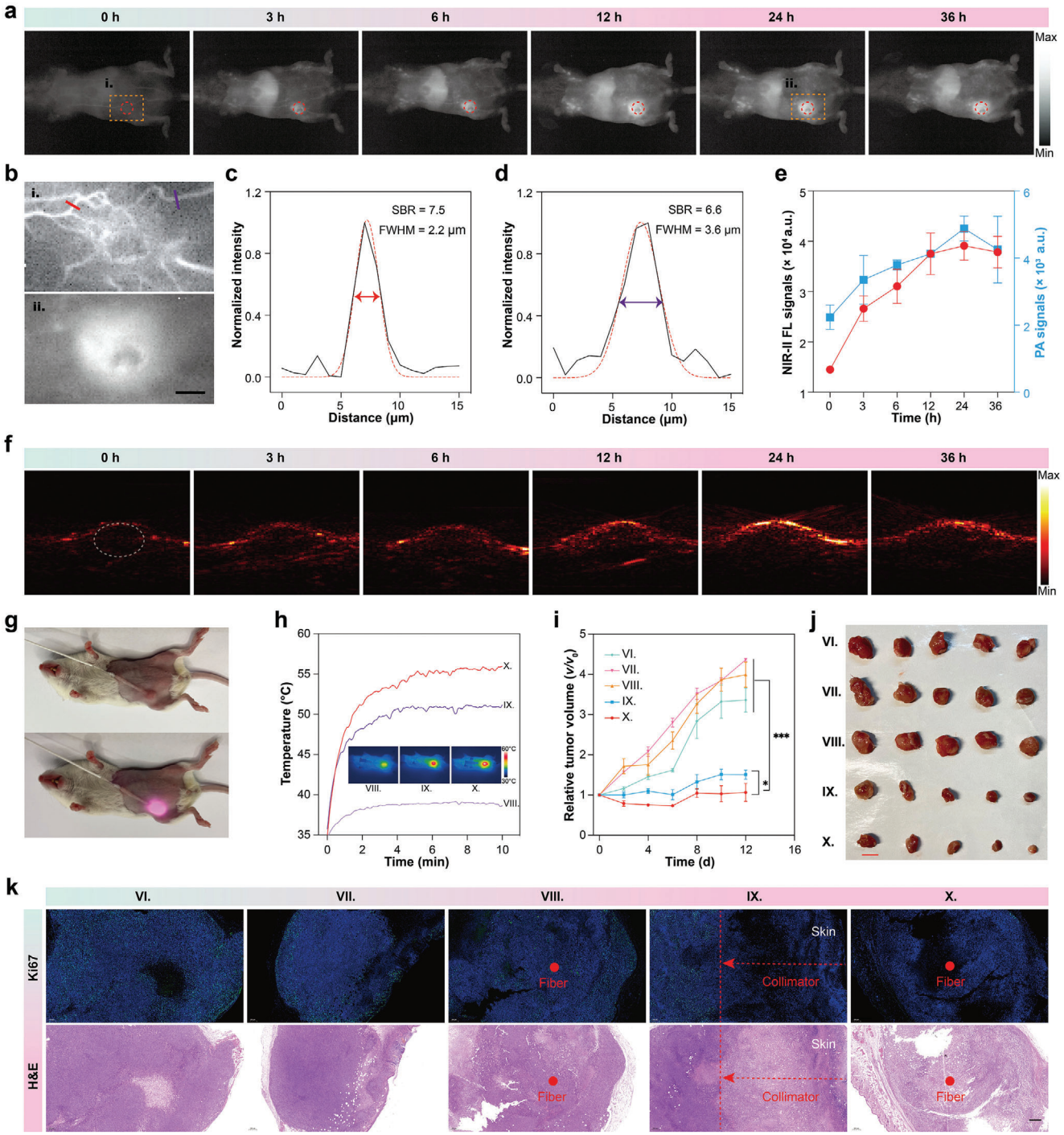

Figure 4. a) Time-dependent NIR-II FLI of 4T1 tumor-bearing mice after intravenous injection of tBuTTBD NPs-iRGD. b) NIR-II FLI of tumor region right after (i) and 24 h post-injection (ii) of tBuTTBD NPs-iRGD. Scale bar: 5 mm. Line profile intensities of selected blood vessels are indicated by c) red and d) purple lines in Figure b-i. e) Average NIR-II FL and PA intensities of tumor tissues at different monitoring times corresponding to panels (a) and (f). f) Time-dependent PAI of 4T1 tumor-bearing mice after intravenous injection of tBuTTBD NPs-iRGD. g) The therapeutic setup of phototherapy guided by a modified optical fiber. h) Temperature variation of tumor sites irradiated with the laser of different treatments. i) Tumor growth curves after various treatments for 12 days (n = 5). j) Images of the tumors after different treatments on day 12. Scale bar: 10 mm. k) Representative Ki67 and H&E-stained images of the tumor tissues in different treatment groups. Scale bar: 200 μm. VI: PBS; VII: tBuTTBD NPs-iRGD; VIII: PBS + NIR laser via a modified optical fiber; IX: tBuTTBD NPs-iRGD + NIR laser via a collimator; X: tBuTTBD NPs-iRGD + NIR laser via a modified optical fiber.

the superiorities of the modified optical fiber in overcoming the limitation in light penetration and realizing larger space for phototherapy.

2.5. Biosafety Assessments of tBuTTBD NPs-iRGD

Considering the importance of biocompatibility for a phototheranostic agent in cancer treatment in vivo, the potential systemic toxicity of tBuTTBD NPs-iRGD was further investigated. First, the hemolysis rate of the NPs was assessed using the diluted erythrocytes. Figure S41 (Supporting Information) demonstrates negligible hemolysis in all groups within a wide range of concentrations from 1 to 100 μM. Such results clearly indicated the bio-inertness of tBuTTBD NPs-iRGD, which is favorable for extending the circulation time in the mouse body and enhancing the targeting of NPs to tumors. Then, tBuTTBD NPs-iRGD of 10 mg kg^{-1} was injected intravenously into healthy BALB/c female mice with mice treated with PBS as a negative control. As illustrated in Figure S42 (Supporting Information), the body weight of the mice in both PBS and tBuTTBD NPs-iRGD treated groups grew steadily and showed negligible discrepancy over two weeks of feeding. It can be concluded that tBuTTBD NPs-iRGD would not induce acute toxicity in healthy mice, reflecting the safe use of the as-proposed NPs. At 15 days postinjection, all mice were sacrificed with the blood and major organs collected for further analysis. As shown in Tables S1 and S2 (Supporting Information), the blood routine and biochemistry indexes appeared normal with no significant difference between PBS and tBuTTBD NPs-iRGD groups, suggesting no obvious systemic side effect toward the immune system, hepatic, and renal functions. Furthermore, the organ coefficient values of the two groups showed no significant difference (Figure S43, Supporting Information), and no apparent organ damage or inflammatory lesions were noticed in all the H&E-stained slices of major organs (Figure S44, Supporting Information). This clearly indicates the excellent biocompatibility of tBuTTBD NPs-iRGD in vivo. All results mentioned above convincingly validated that tBuTTBD NPs-iRGD are promising bio-safe nanomaterials for multimodal phototheranostic bioapplications.

3. Conclusion

In conclusion, this work elucidates an integrated strategy to enable full phototheranostic potential in orthotopic breast cancer treatment. A multimodal phototheranostic AIEgen, namely tBuTTBD, was successfully designed by synchronously realizing efficient intramolecular motions and partial RIM at a highly distorted molecular skeleton with strong D–A relationship, thus showing numerous fascinating features, including maximum absorption at 808 nm, maximum emission at 1092 nm, excellent PA signals, prominent photothermal response, and satisfactory ROS generation. After being formulated into NPs and modified with iRGD, preferential accumulation of tBuTTBD NPs-iRGD in the tumor site was observed according to the trimodal imaging of NIR-II FLI-PAI-PTI. Aiming to implement in situ laser delivery without the light blockage of biological tissues, a modified optical fiber that could efficiently diffuse light was fabricated by splicing a flat-end fiber with an air-core fiber. Accordingly, highly efficient and thorough phototherapy on orthotopic breast tumor-bearing mice was enabled by tBuTTBD NPs-iRGD under laser irradiation guided by a modified optical fiber. This work presents the first example combining multimodal NIR-II emissive AIEgen with interstitial optical fiber for cancer treatment and would trigger state-of-the-art development of phototheranostics in clinical trials.

Supporting Information

Supporting Information is available from the Wiley Online Library or from the author.

Acknowledgements

W.Z. and M.K. contributed equally to this work. The authors acknowledge the financial support from the National Natural Science Foundation of China (62205216, 22105130, 22275124, and 52122317), Basic and Applied Basic Research Foundation of Guangdong Province (2022A1515010381), Basic Research Foundation of Shenzhen (JCYJ20220531101814033 and JCYJ20230808105412024), Medical-Engineering Interdisciplinary Research Foundation of Shenzhen University (2023YG002), Scientific Instrument Developing Project of Shenzhen University (2023YQ008), and Start-up Grant from Shenzhen University (868-000001032015, 868–000001032219, and 868–000001032113). The authors also thank the Instrument Analysis Centre of Shenzhen University for the equipment used. All animal operations complied with the regulations of the Animal Ethical and Welfare Committee of Shenzhen University (AEWC-SZU, Approval No. AEWC-202300019).

Conflict of Interest

The authors declare no conflict of interest.

Data Availability Statement

The data that support the findings of this study are available from the corresponding author upon reasonable request.

Keywords

aggregation-induced emission, molecular design, multimodal phototheranostics, optical fiber, phototherapy

Received: May 6, 2024
Revised: June 30, 2024
Published online: July 26, 2024

[1] a) Z. Zhang, M. Kang, H. Tan, N. Song, M. Li, P. Xiao, D. Yan, L. Zhang, D. Wang, B. Z. Tang, *Chem. Soc. Rev.* **2022**, *51*, 1983; b) G. Feng, G.-Q. Zhang, D. Ding, *Chem. Soc. Rev.* **2020**, *49*, 8179.
[2] a) M. P. Melancon, M. Zhou, C. Li, *Acc. Chem. Res.* **2011**, *44*, 947; b) Y. Liu, P. Bhattarai, Z. Dai, X. Chen, *Chem. Soc. Rev.* **2019**, *48*, 2053; c) Y. Gui, Y. Wang, D. Wang, Y. Qin, G. Song, D. Yan, B. Z. Tang, D. Wang, *Angew. Chem., Int. Ed.* **2024**, *63*, 202318609.
[3] S. He, J. Song, J. Qu, Z. Cheng, *Chem. Soc. Rev.* **2018**, *47*, 4258.

[4] a) J. Cui, F. Zhang, D. Yan, T. Han, L. Wang, D. Wang, B. Z. Tang, *Adv Mater.* **2023**, *35*, 2302639; b) Z. Zhang, W. Xu, M. Kang, H. Wen, H. Guo, P. Zhang, L. Xi, K. Li, L. Wang, D. Wang, *Adv. Mater.* **2020**, *32*, 2003210; c) D. Yan, Z. Zhang, J. Zhang, X. Li, Q. Wu, Y. Gui, J. Zhu, M. Kang, X. Chen, B. Z. Tang, D. Wang, *Angew. Chem., Int. Ed.* **2024**, *63*, 202401877.
[5] C. Chen, H. Ou, R. Liu, D. Ding, *Adv. Mater.* **2020**, *32*, 1806331.
[6] a) M. Fan, Z. Xu, M. Liu, Y. Jiang, X. Zheng, C. Yang, W.-C. Law, M. Ying, X. Wang, Y. Shao, *Appl. Phys. Rev.* **2021**, *8*, 041328. b) Z. Sheng, Y. Li, D. Hu, T. Min, D. Gao, J.-S. Ni, P. Zhang, Y. Wang, X. Liu, K. Li, H. Zheng, B. Z. Tang, *Research* **2020**, *2020*, 4074593.
[7] Z. Xu, Z. Zhang, X. Deng, J. Li, Y. Jiang, W.-C. Law, C. Yang, W. Zhang, X. Chen, K. Wang, *ACS Nano* **2022**, *16*, 6712.
[8] Z. Xu, Y. Jiang, M. Fan, S. Tang, M. Liu, W. C. Law, C. Yang, M. Ying, M. Ma, B. Dong, *Adv. Opt. Mater.* **2021**, *9*, 2100859.
[9] a) Y. Ran, Z. Xu, M. Chen, W. Wang, Y. Wu, J. Cai, J. Long, Z. S. Chen, D. Zhang, B. O. Guan, *Adv. Sci.* **2022**, *9*, 2200456; b) Y. Hu, C. Chi, S. Wang, L. Wang, P. Liang, F. Liu, W. Shang, W. Wang, F. Zhang, S. Li, *Adv. Mater.* **2017**, *29*, 1700448; c) D. R. Sparta, A. M. Stamatakis, J. L. Phillips, N. Hovelsø, R. Van Zessen, G. D. Stuber, *Nat. Protoc.* **2012**, *7*, 12; d) F. Pisano, M. Pisanello, S. J. Lee, J. Lee, E. Maglie, A. Balena, L. Sileo, B. Spagnolo, M. Bianco, M. Hyun, *Nat. Methods* **2019**, *16*, 1185.
[10] a) H. Xie, Z. Bi, J. Yin, Z. Li, L. Hu, C. Zhang, J. Zhang, J. W. Y. Lam, P. Zhang, R. T. K. Kwok, K. Li, B. Z. Tang, *ACS Nano* **2023**, *17*, 4591; b) J. Qi, H. Ou, Q. Liu, D. Ding, *Aggregate* **2021**, *2*, 95.
[11] a) D. Yan, M. Wang, Q. Wu, N. Niu, M. Li, R. Song, J. Rao, M. Kang, Z. Zhang, F. Zhou, D. Wang, B. Z. Tang, *Angew. Chem., Int. Ed.* **2022**, *61*, 202202614; b) H. Li, H. Wen, Z. Zhang, N. Song, R. T. Kwok, J. W. Lam, L. Wang, D. Wang, B. Z. Tang, *Angew. Chem., Int. Ed.* **2020**, *59*, 20371.
[12] a) L. Yang, X. Wang, G. Zhang, X. Chen, G. Zhang, J. Jiang, *Nanoscale* **2016**, *8*, 17422; b) C. Ji, L. Lai, P. Li, Z. Wu, W. Cheng, M. Yin, *Aggregate* **2021**, *2*, e39; c) Z. Zhuang, J. Li, P. Shen, Z. Zhao, B. Z. Tang, *Aggregate* **2024**, e540.
[13] F. Wang, Y. Zhong, O. Bruns, Y. Liang, H. Dai, *Nat. Photonics* **2024**, *18*, 535.
[14] Q. Yang, H. Ma, Y. Liang, H. Dai, *Acc. Mater. Res.* **2021**, *2*, 170.
[15] a) Y. Chen, S. Chen, H. Yu, Y. Wang, M. Cui, P. Wang, P. Sun, M. Ji, *Adv. Healthcare Mater.* **2022**, *11*, 2201158; b) C. Ou, L. An, Z. Zhao, F. Gao, L. Zheng, C. Xu, K. Zhang, J. Shao, L. Xie, X. Dong, *Aggregate* **2023**, *4*, e290.
[16] S. Yang, J. Zhang, Z. Zhang, R. Zhang, X. Ou, W. Xu, M. Kang, X. Li, D. Yan, R. T. K. Kwok, J. Sun, J. W. Y. Lam, D. Wang, B. Z. Tang, *J. Am. Chem. Soc.* **2023**, *145*, 22776.
[17] A. Ji, H. Lou, C. Qu, W. Lu, Y. Hao, J. Li, Y. Wu, T. Chang, H. Chen, Z. Cheng, *Nat. Commun.* **2022**, *13*, 3815.
[18] K. N. Sugahara, T. Teesalu, P. P. Karmali, V. R. Kotamraju, L. Agemy, D. R. Greenwald, E. Ruoslahti, *Science* **2010**, *328*, 1031.
[19] a) Z. Xu, Y. Zhang, W. Zhou, L. Wang, G. Xu, M. Ma, F. Liu, Z. Wang, Y. Wang, T. Kong, B. Zhao, W. Wu, C. Yang, *J. Nanobiotechnol.* **2021**, *19*, 137; b) N. Alifu, A. Zebibula, J. Qi, H. Zhang, C. Sun, X. Yu, D. Xue, J. W. Lam, G. Li, J. Qian, *ACS Nano* **2018**, *12*, 11282; c) S. Gao, G. Wei, S. Zhang, B. Zheng, J. Xu, G. Chen, M. Li, S. Song, W. Fu, Z. Xiao, W. Lu, *Nat. Commun.* **2019**, *10*, 2206; d) S. Song, Y. Zhao, M. Kang, F. Zhang, Q. Wu, N. Niu, H. Yang, H. Wen, S. Fu, X. Li, *Adv. Mater.* **2024**, *36*, 2309748; e) Z. Xu, N. Rao, C.-Y. Tang, C.-H. Cheng, W.-C. Law, *ACS Omega* **2019**, *4*, 14655; f) Z. Xu, R. Aalinkeel, S. D. Mahajan, N. Rao, T. Chen, Y. Jiang, C. Yang, G. Xu, S. A. Schwartz, W.-C. Law, *Adv. Ther.* **2023**, *6*, 2200248.
[20] a) M. Fan, G. Feng, L. Xia, Y. Zhang, M. Liu, Z. Li, Y. Jiang, C. Yang, W. C. Law, K. T. Yong, *Adv. Opt. Mater.* **2023**, *11*, 2300255; b) S. Yang, J. Zhang, Z. Zhang, R. Zhang, X. Ou, W. Xu, M. Kang, X. Li, D. Yan, R. T. Kwok, *J. Am. Chem. Soc.* **2023**, *145*, 22776.
[21] a) K. Wang, X. Zhang, Y. Liu, C. Liu, B. Jiang, Y. Jiang, *Biomaterials* **2014**, *35*, 8735; b) S. Kang, S. Lee, S. Park, *Polymers* **2020**, *12*, 1906.